Carbonates and Evaporites (2025) 40:56
https://doi.org/10.1007/s13146-025-01084-2

ORIGINAL ARTICLE

Petrography image segmentation for analyzing the connectivity of pore networks in Brazilian pre-salt carbonate rocks of the Barra Velha Formation

Herson Oliveira da Rocha[1] · Paulo Edilson Ferreira Moraes[2] · Antonio Abel Gonzalez Carrasquilla[3,5] · José J. S. de Figueiredo[4,5]

Accepted: 21 March 2025

Abstract

This study addresses the challenge of characterizing pore network connectivity within carbonate reservoirs, specifically within the Barra Velha Formation in Brazil's pre-salt deposits. The research aims to determine how effectively digital imaging technology can be used to analyze and quantify the microstructures of these reservoirs. The key questions driving this study are: How well can two-dimensional digital image processing and pore network models capture pores' spatial distribution and connectivity? To what extent do these methods correlate with other petrophysical properties critical to reservoir performance? To answer these questions, we evaluated the petrophysical and geometrical characteristics of the pore system using various distance metrics—Euclidean, Quasi-Euclidean, City-block, and Chessboard—to assess pore connectivity. The study found that while digital image analysis provides valuable insights, its effectiveness depends heavily on the chosen distance metric and the specific properties of the carbonate reservoir. The results suggest that the Euclidean and Quasi-Euclidean metrics are more reliable for capturing connectivity in these settings, offering clues for better understanding fluid dynamics and improving exploration and extraction strategies. However, the study also reveals limitations in the digital approach, particularly in its ability to fully capture the complexity of the pore network. These findings confirm the relevance of digital imaging but also underscore the need for more advanced methods or complementary techniques to achieve a more accurate characterization of carbonate reservoirs.

Keywords Pore network connectivity · Digital imaging process · Carbonate reservoirs · Pre-salt deposits · Petrophysical analysis

✉ Herson Oliveira da Rocha
herson.rocha@macae.ufrj.br

[1] Polytechnic Institute (IPOLI), Federal University of Rio de Janeiro (UFRJ), Avenue Aluízio da Silva Gomes, S/N, 27930-560 Macaé, RJ, Brazil

[2] Faculty of Engineering (FAE), Federal University of Para (UFPA), Rua Raimundo Santana Cruz, S/N, 68721-000 Salinopolis, PA, Brazil

[3] Laboratory of Petroleum Engineering (LENEP), Science and Technology Center (CCT), Northern Rio de Janeiro State University (UENF), Amaral Peixoto Road, Km 163, Av. Brennand S/N, Imboassica, 27925-310 Macaé, RJ, Brazil

[4] Laboratory of Petrophysics and Rock Physics (LPRP) Prof. Dr. Om Prakash Verma, Faculty of Geophysics (FAGEOF), Federal University of Para (UFPA), Rua Augusto Correa, 01, 66075-110 Belem, PA, Brazil

[5] National Institute for Petroleum Geophysics (INCT-GP), 40170-115, Avenue Milton Santos, S/N, Salvador, BA, Brazil

Introduction

Imaging techniques are becoming increasingly valuable for analyzing the structure of small objects, particularly in three dimensions. At the same time, numerical models for calculating transport properties through these structures based on experimental images are developing rapidly (Bultreys et al. 2015, 2016). Various digital image analysis (DIA) techniques have evaluated the petrophysical and geometrical properties of the pore system in two dimensions (2D) to date. These methods have also successfully identified larger and medium-sized pores (Neto et al. 2018; Da Rocha et al. 2019). One essential method for modeling the hydraulic behavior of porous media at the microscale is porous network modeling (Raoof and Hassanizadeh 2010).

Network models can predict various petrophysical features by depicting the voids in a rock as a lattice of

Published online: 20 April 2025

interconnected pores and throats (Dong and Blunt 2009). The imaging accuracy and the network's correspondence to the natural porous rock determine how reliable network models are (Sheppard et al. 2004; Sok et al. 2002).

there has been a concentrated effort in research to enhance conventional network modeling techniques for examining carbonate reservoirs. Researchers have devised a novel multi-scale imaging technique to improve the comprehension of carbonates' pore structure and connectivity (Sok et al. 2002). The method used images from micro-computed tomography, focused ion beams, and backscatter scanning electron microscopy (Bernabe et al. 2010; Raoof and Hassanizadeh 2010; Sok et al. 2010; Gharbi et al. 2012; Rabbani et al. 2014) that were both three-dimensional (3D) and two-dimensional (2D).

Ioannidis and Chatzis (2000) developed a dual network model that accounts for connected channels in vuggy carbonates by superimposing them on the matrix. They compared the model predictions with measurements of capillary pressure. Dong and Blunt (2009) looked at four ways to extract and rebuild networks using 3D images of sandstones and carbonates. These were the median axis, velocity-based, grain detection, and maximum ball algorithms. In water-wet cases, the relative permeability predictions for water floods showed a similar behavior to carbonates. They concluded that maximum ball extraction and velocity-based algorithms generally provide similar predictions for multiphase properties.

Raoof and Hassanizadeh (2010) developed a novel technique for creating a multidirectional pore network that accurately represents a porous medium. The method employs a standard cubic lattice consisting of two components: pore bodies positioned at regular lattice points and a network of pore throats connecting these pore bodies. The method's results strongly agreed with simulations and empirical data, showcasing the distribution of coordination numbers and other network properties, such as the average coordination number and the count of pore bodies and pore throats.

Van der Land et al. (2013) have shown how pore-scale models representing typical carbonate sediments and their diagenetic history can quantify the evolution of petrophysical properties in carbonate rocks. The 3D pore architecture models (i.e., the spatial distribution of solids and pores) created from binarized 2D images showed how the structure and texture of carbonate sediments change over time.

Based on micro-computed tomography (micro-CT), Bultreys et al. (2015) developed a novel dual pore network model (DPNM), which accounts for microporosity in a highly scaled manner using symbolic network elements called micro-links while treating macroporosity as a conventional pore network model. Local information from micro-CT scans determines the connectivity and conductivity of the microporosity. The macropore network allows the microporosity to connect in parallel and series.

Huang et al. (2021) formulated a technique to assess permeability by quantifying the number of pores, cracks, and vugs in two-dimensional pictures and Valentin et al. (2018) estimated absolute permeability of fissured-vuggy carbonate by looking at how the pore area was distributed in the 2D images within a set statistical range. The primary obstacle lies in accurately identifying whether an empty cavity corresponds to a pore or a throat to analyze and streamline the 2D digital image processing datasets. While separating the continuous and interconnected empty spaces of porous media into distinct pores and throats is challenging, some simplifying assumptions must be applied (Rabbani et al. 2015).

Khan et al. (2022) conducted a series of experiments on Ambela granite at predetermined temperatures to analyze the impacts of increasing temperature on porosity. It was possible to note the effects mediated by increasing temperature on granite damage, which was significantly greater during rapid cooling, resulting in a significant decrease in uniaxial strength and Young's modulus. In this context, a composite criterion is used for thin-section study and, based on our results, a new model, predicted in watershed segmentation, which is an image processing technique to capture the effect of thermal heat on porosity, cracks, and damage factor, was numerically simulated.

A procedure based on recently provided geoscience data was integrated by Ghanbarnejad Moghanloo and Riahi (2023) to evaluate the reservoir characteristics and structural interpretation of the highly prolific Burgan formation in the Abadan plain, SW Iran. The new high-resolution SEM pictures were used to assess the Burgan formation's pore size, distribution, and aspect ratio. Moreover, the watershed segmentation method could identify closed pores and mouths. The porosity log at many well sites was calibrated to undertake petrophysical modeling using the porosity fractions obtained from SEM images.

Alatrash and Velledits (2024) investigated the pore network of four carbonate rock samples originating from an oil well in Hungary. Two samples were from the productive part of the Sarmatian limestone, and the other two were from the dry interval. Was employed X-ray computed tomography (micro-XCT) in combination with lab measurements and microfacies analysis. The comparison between the measured helium porosity and image-derived porosity showed a close match. Micro-XCT measurements revealed connected pore structures in the productive interval, compared to isolated pores in the dry interval.

This study shows a computer algorithm for automatically extracting pore network features that show the natural structure of pores and throats, based on work by Rabbani et al. (2014) and Rocha and Carrasquilla (2021). Using two well-known image processing algorithms together—the distance

function and watershed segmentation—this method directly finds and separates pores and throats. It does this on a 2D image from samples of pre-salt carbonate reservoirs in the Santos Basin, Brazil.

Geological overview of the Brazilian Santos Basin: evolution and characteristics

The Brazilian Santos Basin, strategically located between the Campos and Pelotas Basins, is a geologically rich region with clear boundaries defined by the Alto de Cabo Frio to the north and the Alto de Florianopolis to the south. The Neocomian era, when the Gondwana supercontinent broke apart and the Atlantic Ocean opened, formed this important passive margin basin (Macedo 1989).

The sedimentary section in the Santos Basin, which reaches a considerable thickness of up to 15 km, comprises rift sequences and reflects the dynamic geological processes during the separation of the South American continent. Marginal depressions formed in the Pelotas, Santos, and Campos basins, forming a unique sedimentary layer with a cap layer and transitional and marine phases (Mio 2005) (Fig. 1).

Geologically, the Santos Basin divides the Barra Velha Formation into three super-sequences: post-rift, rift, and drift. The post-rift phase further subdivided into upper and lower sequences, features a variety of deposits such as microbial limestones (LIMs), stromatolites (STRs), laminites (LMTs), shales schists, grainstones (GSTs), wackestones (WKTs), and packstones (PKTs). The upper sequence, from the Late Aptian period, has STRs, LIMs, and dolomitized microbial LMTs (Modica and Brush 2004; Moreira et al. 2007).

The rift phase began in the Cretaceous and culminated with the opening of the South Atlantic Ocean. The Santos Basin evolved from small grabens to extensive lagoons and

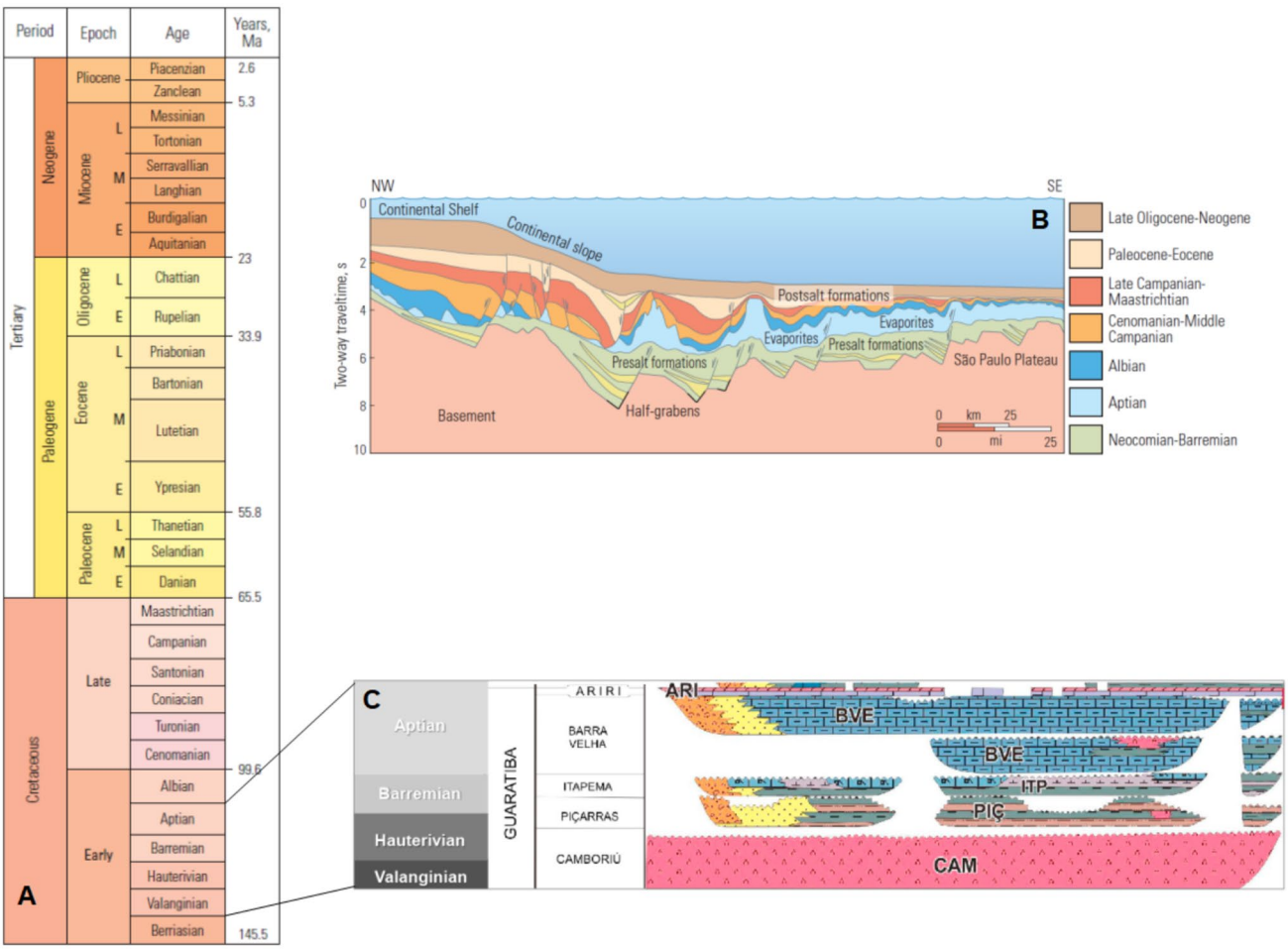

Fig. 1 Characteristics of the Geology of the Santos Basin: A stratigraphic column depicting the basin's layers (**A**), emphasizing the continental margin highlighting pre-salt source rocks and overlying carbonate reservoirs targeted beneath a thick layer of evaporites (**B**). Additionally, the focus is on the Camboriu Formation (CAM), Piçarras (PIÇ), Itapema (ITP), Barra Velha (BVE), and Ariri (ARI), respectively (**C**) (Adapted from Modica and Brush, 2004; Moreira et al. 2007)

lakes in a broader regional context. The lacustrine carbonates form in the lakes in response to various environmental factors such as salinity, pH, water level, topography, and sediment composition.

The resulting carbonate rocks have different pore sizes and types, with diagenesis critical to the quality and the depositional texture. The main geological events that affected the Brazilian pre-salt reservoirs, and specifically the reservoir strata, began with the rifting process that separated the South American and African continents during the Jurassic and Early Cretaceous, creating rift basins where clastic and carbonate sediments were deposited. During the Early Cretaceous, following the initial separation, a shallow marine environment conducive to the deposition of carbonates, including stromatolites and other biogenic structures, dominated the region. These carbonates form the primary reservoir rock in the pre-salt. The Aptian marine transgression led to the deposition of a thick sequence of evaporites (mainly salt). These salt layers are crucial as they act as effective seals for hydrocarbon reservoirs. After the deposition of evaporites, salt tectonics played a significant role, with salt deforming and creating structures such as salt domes and diapirs. These structures influence hydrocarbon migration and accumulation in the underlying reservoirs. Continuous tectonic activity during the Late Cretaceous and Cenozoic caused faulting and reactivation of structures, which could impact fluid migration and reservoir compartmentalization (Riding and Liang 2005; Borghi and Corbett 2013; Faria et al. 2017).

These events combined resulted in the complex current architecture of pre-salt reservoirs, characterized by high porosity and permeability, and the presence of hydrocarbons at significant depths, covered by thick salt layers. Diagenesis has significantly impacted the pore networks in the Brazilian pre-salt reservoirs through several processes, such as cementation, where precipitation of minerals like calcite and dolomite within the pore spaces has reduced porosity and permeability. Partial dissolution of minerals has increased secondary porosity, enhancing reservoir quality in some areas. Mechanical compaction due to overburden pressure has decreased pore volume and connectivity. Mineral replacement, where original minerals transform into new minerals (e.g., aragonite to calcite), either enhanced or diminished porosity depending on the conditions. These diagenetic processes collectively alter the pore structure, influencing the storage and flow characteristics of the hydrocarbons within the reservoir. The pre-salt carbonate mineralogy in the Santos Basin consists mainly of limestone, dolomite, and silica. It also contains magnesium-rich clays, stevensite, and heavy minerals like pyrite (Azevedo et al. 2021; Wennberg et al. 2023; Strugale et al. 2025).

Classifying the pore structure of granular dolomite and microbial dolomite involves analyzing the characteristics of the pores, such as their size, shape, distribution, and connectivity. The pore structure in granular dolomite is often dominated by intergranular pores. These pores exist between the dolomite grains. The pore sizes can vary but are generally larger and more uniformly distributed compared to microbial dolomite. The pores are typically more equant or rounded, reflecting the spaces between well-sorted grains. The connectivity of pores in granular dolomite tends to be higher due to the larger, more interconnected pore spaces. This results in better permeability.Granular dolomite forms in high-energy environments where grains are well-sorted, leading to a more open and connected pore system (Land 1985; Wright 1999).

While the microbial dolomite features a more complex pore structure, often including intramicritic and vuggy pores. These pores can form within or between the microbial framework. The pores in microbial dolomite are often smaller and more variable in size. They can range from micro to mesopores, with some larger vugs. The shapes of pores in microbial dolomite are often irregular, reflecting the microbial activity and subsequent dolomitization. The connectivity in microbial dolomite can be lower compared to granular dolomite due to the more complex and irregular pore network. This can result in lower permeability. Microbial dolomite forms in environments influenced by microbial activity, which creates a unique pore structure as microbes and organic matter are replaced or encased by dolomite (Land 1985; Wright 1999).

Theoretical development and methodology

Image processing and pore connectivity analysis

Da Rocha et al. (2019) used image processing on ten petrographic samples from a Brazilian pre-salt reservoir in the Santos Basin, Brazil, to examine how pore network coordination number affects permeability. It quantifies the number of neighboring pores connected to a given pore through pore throats. This parameter is significant in understanding fluid flow and permeability in reservoir rocks. A higher coordination number indicates better connectivity, which can enhance fluid flow and reservoir performance. In contrast, a lower coordination number suggests isolated pores, which can hinder fluid movement and reduce permeability.

The number of surrounding pores connected through pore throats determines the coordination number of a pore. Multiple studies have demonstrated that its influence is equally or even more substantial than that of porosity (Jivkov et al. 2013; Rabbani et al. 2014; Rocha and Carrasquilla 2021). However, the approximation represents the mean value across the entirety of the pore space. Furthermore,

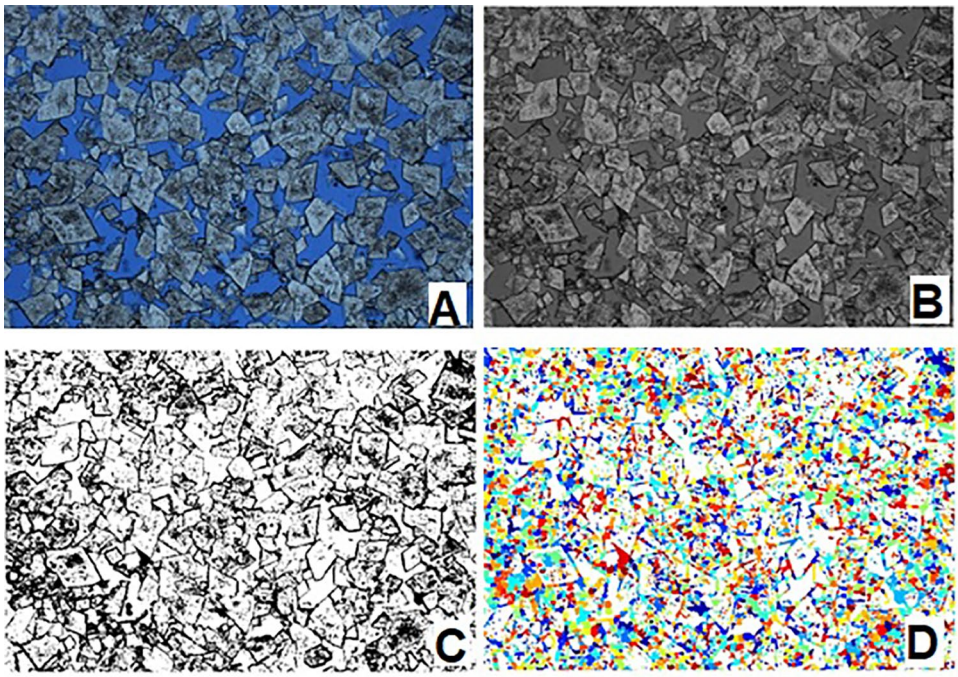

Fig. 2 Description of the steps performed during the processing of petrographic images. **a** The figure shows, from left to right: the original image in RGB scale, capturing the real colors; **b** the image converted to grayscale, highlighting the light intensity of the pixels; **c** the binarized image, where the pixels were classified into two levels (black and white) based on an intensity threshold; and **d** the segmented image, in which different regions or objects were identified and separated for specific analysis

calculating pore roughness as pore throats can yield unreliable results.

Here, it is important to convert the initial 2D image (RGB true color) into a grayscale intensity (gray color) by eliminating hue and saturation characteristics while preserving brightness. The image is represented by a 2D array with dimensions [m, n, p], where m and n indicate the size of the array, and p denotes the range of potential values from 0 to 255. Matrix A in Eq. (1) represents this array.

The grayscale image is then converted into a binary image. The histogram of the grayscale image's intensity is analyzed to select the optimal threshold. The Otsu method (1979) was employed in this binarization process, effectively separating pixels into two groups (light and dark). This method automatically determines the ideal threshold by minimizing intra-class variance, which means reducing the difference within the light and dark pixel groups while maximizing their separation. This approach is particularly useful when the image has a bimodal intensity distribution (see Fig. 2).

The binarized image is generated by assigning a value of 1 (representing white) to all pixels in the input image that have a brightness greater than the given threshold, and a value of 0 (representing black) to all other pixels. To convert the image from RGB to grayscale and subsequently binarize it, the rgb2gray, im2bw, and imbinarize functions of the Matlab software were used. The binarized image is represented by the matrix B in Eq. (2), with values ranging from 0 to 1. The specified range corresponds to the possible signal levels for the image category, as indicated by Jahari et al. (2021).

Therefore, it is crucial to calculate a specific threshold (level) for each image, based on your lithology, that may be used to convert an intensity image into a binary image. The graythresh function calculates this level using the Otsu threshold selection method which also was employed to decrease the disparity between black and white pixels and calculate the distance transform. The distance transform of a binary image is an essential operation in the field of image processing (Tawfeeq and Al-Sudani 2020).

The distance transform assigns a value to each pixel based on its proximity to the borders of an object. Edges or contours in a grayscale image are typically defined as regions where there is a significant change in intensity or brightness. These changes are detected using edge detection algorithms that calculate the image gradient's magnitude to identify areas with the strongest intensity gradient.

To find edges, was used the edge function. This function looks for places in the image where the intensity changes rapidly, using one of these two criteria: (i) places where the first derivative of the intensity is larger in magnitude than some threshold and (ii) places where the second derivative of the intensity has a zero crossing. This process emphasizes boundaries between objects or regions, providing crucial spatial information for analyzing structural features and spatial relationships within the image. The segmented image displays distinct hues that arise from the matrix representation of matrix C in Eq. (3), as defined by:

$$A = \begin{bmatrix} 255 & 201 & 194 & & 78 & 199 & 246 \\ 189 & 36 & 36 & \cdots & 45 & 91 & 54 \\ 96 & 59 & 19 & & 255 & 100 & 250 \\ & \vdots & & \ddots & & \vdots & \\ 89 & 121 & 65 & & 123 & 76 & 171 \\ 111 & 90 & 240 & \cdots & 57 & 210 & 149 \\ 56 & 12 & 130 & & 255 & 254 & 143 \end{bmatrix}, \quad (1)$$

$$B = \begin{bmatrix} 1 & 1 & 1 & & 0 & 0 & 1 \\ 1 & 0 & 0 & \cdots & 0 & 0 & 0 \\ 0 & 0 & 0 & & 1 & 0 & 1 \\ \vdots & & & \ddots & \vdots & & \\ 0 & 0 & 0 & & 0 & 0 & 1 \\ 1 & 0 & 1 & \cdots & 0 & 1 & 1 \\ 0 & 0 & 1 & & 1 & 1 & 1 \end{bmatrix}, \quad (2)$$

and

$$C = \begin{bmatrix} 0.00 & 0.00 & 1.00 & & 0.00 & 2.00 & 3.00 \\ 0.00 & 0.00 & 0.00 & \cdots & 1.42 & 1.36 & 3.00 \\ 1.00 & 1.00 & 1.41 & & 0.00 & 1.00 & 2.24 \\ & \vdots & & \ddots & & \vdots & \\ 1.00 & 1.00 & 1.00 & & 1.41 & 2.00 & 3.00 \\ 1.41 & 1.00 & 1.41 & \cdots & 1.00 & 1.00 & 1.41 \\ 1.00 & 0.00 & 0.00 & & 00.0 & 0.00 & 1.00 \end{bmatrix}. \quad (3)$$

The process begins with calculating the distance transformation of the binary image after its inversion. This procedure is followed by a modification step, ensuring the background is transformed into an independent watershed. Subsequently, the watershed transformation recognizes discrete sections within the image, resulting in a comprehensive segmentation representation. Due to its fast and effective method, the watershed algorithm was used to subdivide and separate groupings of attached objects. The watershed image segmentation method was used to divide the sample matrix into segments. Thus, the algorithm was adapted to optimize the transfer of rock networks by setting a threshold determined by the average intensity of the grains (Gostick 2017).

However, a significant challenge arises when applying the watershed approach to the image edges. A conventional edge image generation technique that involves the application of a gradient was proposed to address this issue. Then, the resulting gradient image was constrained to obtain a binary edge image. The main challenge of this method is choosing the most favorable threshold value (Kumar and Anuradha 2017).

The suggested algorithm is applied to the 2D images of the samples to begin segmenting porous media and extracting the network. The algorithm aims to divide grains and pores and throats.

Figure 2 depicts the complete sequence of procedures involved in digital image processing and analysis for petrographic pictures. The watershed segmentation algorithm can identify and isolate pore bodies in 2D and 3D pictures. To avoid unnecessary complications, we present a simplified explanation in 2D, which can expand to 3D using a comparable methodology when considering two objects in physical contact (Gonzales et al. 2004).

The watershed segmentation algorithm is employed to identify and isolate these interconnected components. Before creating the distance map (see Fig. 3A, B), it is necessary to transform the binary picture using the distance function. The distance between a pixel and the nearest pixel on the object boundary determines its brightness in the distance transformation surface (Sonka et al.2014). The next step involves constructing a topological surface using the distance map. The more intense pixels correspond to the lower regions of the generated (see Fig. 3C).

Consequently, a basin is formed for every object that encounters each other in the image. When executing the watershed algorithm, precipitation is assumed in both basins. According to the depth contours, water accumulates in the lowest part of the basins (see Fig. 3D). The water level in the basins increases until the two distinct bodies of water meet. The watershed ridgeline corresponds to the pixels where the streams from two basins meet. All watershed ridgeline locations are identified by extrapolating the extent of flooding.

The watershed ridgeline separates the two adjacent objects interpreted as pore bodies. The associated pore roughness are subsequently determined by examining the pixels forming the pores' boundaries. The ball-and-stick model can be used to visualize the pore network by representing pores as spheres (balls) and the connections

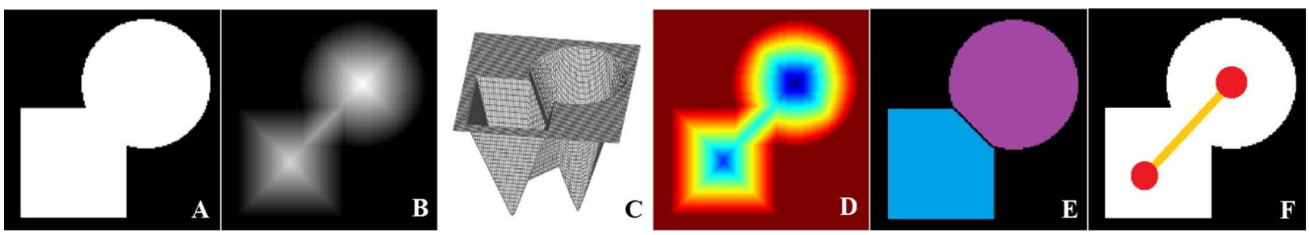

Fig. 3 Workflow for sample segmentation using the watershed method. **a** the original binary image, **b** the grayscale distance map, **c** the topological surface, **d** depth contours, **e** detected objects separated by watershed ridgeline, and **f** the ball-and-stick model (Rabbani and Ayatollahi 2015)

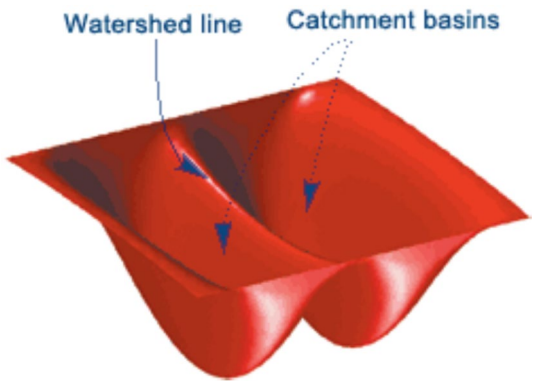

Fig. 4 Schematical model of the topological surface of the catchment basins and watershed lines

between them as sticks, providing a clear depiction of the network's structure and connectivity, as shown in Fig. 3E, F.

Figure 4 illustrates the operational mechanism of the watershed algorithm, which produces an array of labels that identify the distinct watershed regions included in the input array. This technique functions on arrays of arbitrary dimensions, identifying "catchments" or "ridge lines" within a picture (Rabbani et al. 2014).

In this approach, the image is a flat area where bright pixels symbolize high elevations and dark pixels signify low altitudes. The elements of the matrix in the image are integers that are equal to or larger than 0. This development allows for accurately identifying different locations (Mandzhieva and Subhankulova 2021).

Elements with a designation of 0 do not belong to any single watershed region. The items labeled with the number 1 belong to the first watershed region, whereas the elements labeled with the number 2 belong to the second watershed region, and so on. The default setting for the watershed algorithm is eight connected neighbors for 2D images and 26 connected neighbors for 3D inputs.

The neighborhood of a pixel consists of adjacent pixels in specific directions, determining their connectivity. In 2D, pixels are connected if their edges touch, with a neighborhood connectivity of 4 or 8. In 3D, the central pixel is linked to adjacent pixels in six directions (in, out, left, right, up, down) with a connectivity of 6, or with a connectivity of 18 when combining directions (Meyer 1994).

Finally, the connectivity score is 26, indicating that pixels are related if their faces, edges, or corners come into contact. The pixel's neighborhood consists of the surrounding pixels in the directions of inside, outside, left, right, up, and down. Combining two directions, like downward to the right or upward to the right, forms a compound direction. A combination of three directions, such as right up or left down, refers to the simultaneous connectivity in two perpendicular directions.

Analyzing the adjacent pores and throats and counting the number of throats connected to each pore provides a straightforward method to determine the coordination number or connectivity of the pore network. Pore connection is a critical factor determining a porous material's hydraulic properties. Elements labeled as 0 are not associated with any specific watershed region. The things marked with the numeral 1 refer to the initial watershed region, whereas the elements marked with the numeral 2 refer to the subsequent watershed region, and so on (Singh et al. 2021).

The default configuration for the watershed algorithm includes eight connected neighborhoods for 2D pictures and 26 connected neighborhoods for 3D inputs. The pixel's neighborhood is defined as the collection of nearby pixels in the horizontal or vertical direction, as depicted in Fig. 5 (Meyer 1994).

Additionally, it can encompass a dual-orientation, such as a rightward and downward direction, with connectivity of 18. The images are segmented into pores, and a topologically representative network of pores and throats is extracted from these images. The distance function calculates the distance between each pixel in the void of the porous medium and the nearby pixel occupied by the solids. The distance function occurs in four different forms of contour line or plane generation: (a) Euclidean, (b) city-block, (c) checkboard, and (d) quasi-Euclidean

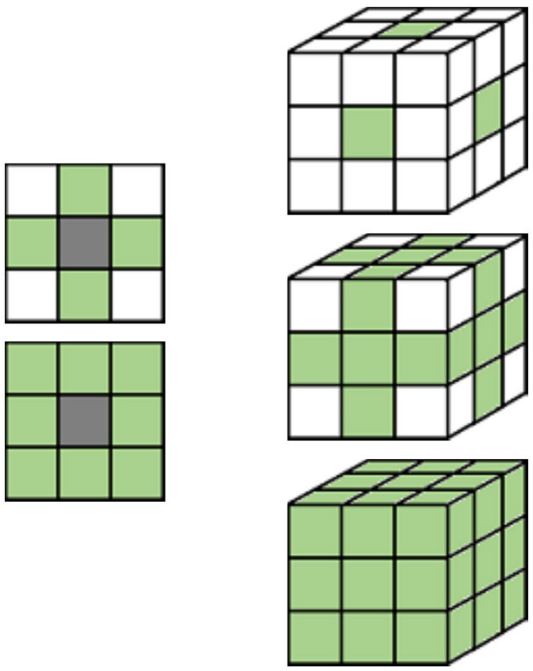

Fig. 5 Model of pixel connectivity. The default connectivity is 8 for 2-D images (left) and 26 for 3-D images (right)

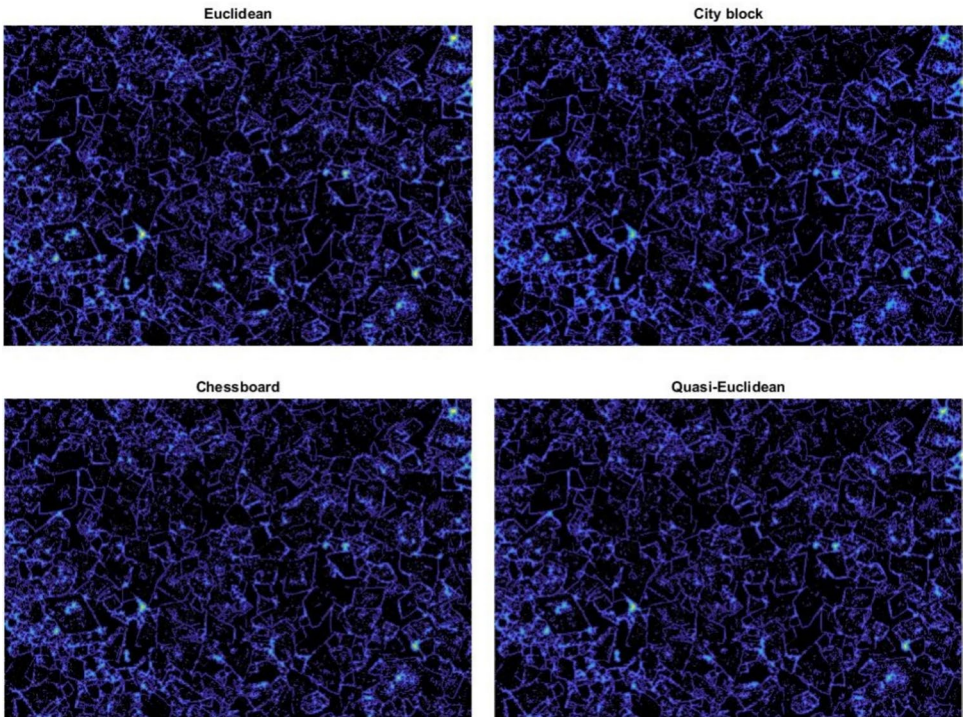

Fig. 6 The four different forms of distance functions for 2-D porous structures, where the distance transform provides a metric or measure of the separation between points in the image. From left to right and clockwise, have the distance functions Euclidean, City-block, Quasi-Euclidean, and Chessboard

(Rosenfeld and Pfaltz 1966; Rabbani et al. 2014; Kumar and Anuradha 2017; Maurer Jr et al. 2023) (see Fig. 6).

Equations 4–7 show the distance transformations (d) calculation for the Euclidean, city-block, chessboard, and quasi-Euclidean methods, respectively. The chessboard distance between two different points (x_1, y_1) and (x_2, y_2) is:

$$d = max\left(|x_1 - x_2|, |y_1 - y_2|\right). \tag{4}$$

The city-block distance between (x_1, y_1) and (x_2, y_2) is:

$$d = |x_1 - x_2| + |y_1 - y_2|). \tag{5}$$

The Euclidean distance between (x_1, y_1) and (x_2, y_2) is:

$$d = \sqrt{(x_1 - x_2)^2 + (y_1 - y_2)^2}. \tag{6}$$

The quasi-Euclidean distance between (x_1, y_1) and (x_2, y_2) is:

$d = |x_1 - x_2| + \left(\sqrt{2} - 1\right)|y_1 - y_2| O$ therwise, if $|x_1 - x_2| > |y_1 - y_2|$

$$d = \left(\sqrt{2} - 1\right) + |x_1 - x_2| + |y_1 - y_2|. \tag{7}$$

The distance transform provides a metric or measure of the separation of points in the image. The function calculates the distance between each pixel set to off (0) and the nearest non-zero pixel for binary images (see Table 1).

Description of core samples

The lithologic description, texture, and occurrence of the primary pore type were carried out according to Dunham (1962), Lucia (1995), and Riding and Liang (2005). The stratigraphic characteristics of the reservoir are listed in Table 2. The petrophysical characteristics and photomicrograph characteristics are shown in Table 3.

The samples are representative of carbonate facies within a depositional environment that experienced significant diagenetic alterations, including cementation, dissolution, and recrystallization. The porosity types observed—ranging from intercrystalline to vugular -suggest varying degrees of reservoir quality, influenced by both primary depositional textures and subsequent diagenetic overprints.

The presence of organic material and siliciclastic components further indicates a dynamic depositional environment, possibly linked to fluctuating energy conditions and chemical diagenesis. The overall reservoir potential varies, with some samples showing good connectivity and porosity, while others are more limited due to extensive cementation and porosity ranging from low to moderate.

Results and discussions

Figure 7 shows that the contour lines that mark the boundary between the two pores exhibit substantial variations for differentiating between pores and throats in a rock

Table 1 The description of distance metrics mentioned in Eqs. (4) to (7)

Distance Metric	Description	Illustration
Euclidean	The Euclidean distance is the straight-line distance between two pixels	
City-block	The City-block distance metric measures the path between the pixels based on a 4-connected neighborhood. Pixels whose edges touch are 1 unit apart; pixels diagonally touching are 2 units apart	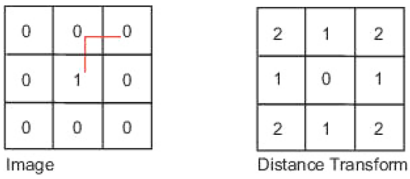
Chessboard	The Chessboard distance metric measures the path between the pixels based on an 8-connected neighborhood. Pixels whose edges or corners touch are 1 unit apart	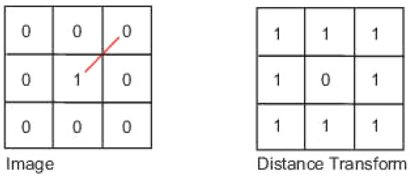
Quasi-Euclidean	The Quasi-Euclidean metric measures the total Euclidean distance along a set of horizontal, vertical, and diagonal line segments	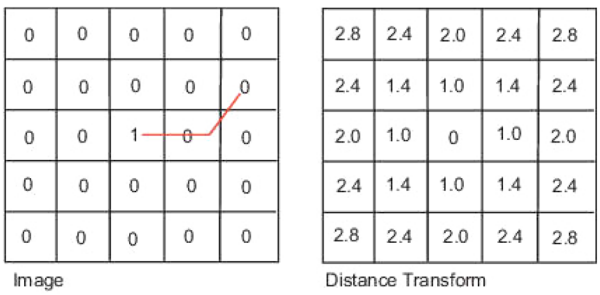

sample [A] (see Fig. 7F). Subsequent examinations and additional investigations have demonstrated that while the chessboard shape is appropriate for this sample, it is not optimal, because where the distance between pixels may need to account for diagonal adjacency, this metric can not contour the pores. By intersecting with curving pore walls, the angular and cubic geometries of the city-block and checkerboard patterns provide clear boundaries and enhance the differentiation between pores and throats. The inflection points observed in the shape of the contours in the city-block and checkerboard images correspond to the highest points of the watershed.

Connecting the dots can reveal clusters or blocks of non-zero components in the dispersion patterns, indicating an underlying structure in the data. The breakpoints, which are evident in the curvature of the contours in the block and checkerboard pictures, indicate the highest points of the watershed crest line. These points were produced by connecting the points generated in the connection matrix (Fig. 7I). Figure 7J illustrates the interconnection of the pores. The pore network has a one-modal distribution, with a clear peak between 4 and 5 connections between the pores.

The results obtained from samples [B], [C], and [D] exhibit no significant variation compared to the results obtained from sample [A] (see Figs. 8, 9, 10). The segmentation technique in these diverse carbonate samples enabled examining their pore network (see Figs. 8D, 9D, and 10D).

This process is evident from the matrices' plots, which reflect the sparse adjacency matrix of the points in the connection graph (see Figs. 8I, 9I, and 10I). Histograms show the frequency distribution of coordination numbers to identify the pores' connectivity. The result indicates that sample [B] has a concentration of pores with four connections (Fig. 8J). On the other hand, samples [C] and [D] have pores with three connections, and their distribution is asymmetric towards the right, as shown in Figs. 9J and 10J.

The chessboard format was the most appropriate method of measuring distance in sample [E] (see Fig. 11) because the distance between pixels in this sample takes diagonal adjacency into account, especially for tasks such as image feature extraction, such as organic matter identification. The sparse adjacency matrix in Fig. 11I shows that the points in the connectivity graph are spread out more evenly than in samples [A] to [D]. This event is associated with an

Table 2 Summary description of the 10 samples used in this study based on the geological description of the main photos and thin sections

Samples	Core photos	Thin sections	Description
[A]		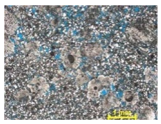	The sample consists of simple spherulites with a well-defined dark core, dispersed in a dolomite matrix composed of small crystals associated with dark material, potentially of organic origin. The microfabric includes spherulites as the main constituent and spherules as secondary components. Porosity is characterized as vugular and moldic
[B]			Formed predominantly by spherulites of varying sizes with arbustiform elements, "floating" in a "dirty" microcrystalline limestone with spherules. Note also the presence of a crust of broken silica formed essentially by chalcedony with moderate intensity degree, with rare microcrystalline aggregates and vugular porosity
[C]		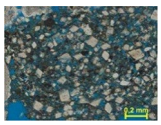	The rock is partially cemented by medium to thick rhombohedrons of dolomite and locally cemented by quartz crystals, presenting moderate porosity of the intercrystalline, interelements, intraelements, intracrystalline and vuggy types
[D]			The stromatolite presents moderate porosity, of the types intercrystalline, interelements, intraelements, intracrystalline associated with the dissolution of dolomite. In detail the recrystallization and dissolution of the element generating porosity of the intraelement type
[E]		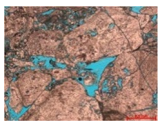	It occurs locally microfractures in the elements, cemented by dolomite rhombohedral block, with porosity varying from moderate to good, of types intraelement, intercrystalline and fracture
[F]		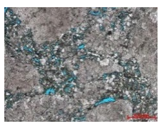	The spherulitic structure of the rock has a porosity of the intercrystalline type, related to the dissolution of both the matrix and the element originating from the dolomite cementation process and later by the element recrystallization
[G]			The laminite presents incipient lamination, associated with the dissolution of the micritical matrix and replacement of the matrix with quartz. In particular the very low porosity of the intercrystalline type
[H]		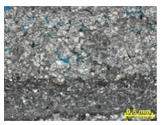	The rock presents intense cementation and replacement by rhombohedral dolomite crystals ranging from fine to medium and punctually by thin anhedral quartz with remnants of clayey associated with dolomite. It presents very low porosity, predominantly of interelemnts types and intercrystalline caused by the presence of dissolution films evidencing chemical compaction
[I]			Thin spherulite laminate formed by the alternation of larger spherulite slides and smaller spherulite slides, spherules, dolomite, organic matter, and siliciclastic (rare), and some spherulites were dissolved. It has low porosity of the vugular and motile types
[J]		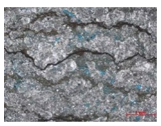	The sample is characterized as spherulitite with dolomite and a spherulitic structure. Primary constituents are spherulites, and secondary constituents are arbustiform elements. The composition is primarily dolomite, displaying a micritic texture with agglutinated elements. Porosity types include intercrystalline, interelement, and intraelement. Key diagenetic events involve intense replacement and recrystallization of spherulites by dolomite, dolomite cementation with single and mosaic textures in interelement pores, weak dissolution, quartz cementation, mechanical and chemical compaction, and further dissolution

alteration in lithology within a specific portion of the reservoir. Like the packstones, samples [C] and [D] show a clear micritic or clayey matrix between the grains. However, sample [E] of the grainstones has little to no matrix (Table 3).

Table 3 presents the samples' principal petrophysical properties and the characteristics of photomicrographs in the thin sections. These data demonstrate that the depositional environment directly influences porosity and permeability values, as well, as high-energy environments typically yield grainstones, whereas moderate-energy environments tend to form packstones.

Table 3 Resume the principal petrophysical properties of the sample and the characteristics of photomicrographs in the thin sections

Sample	Depth (m)	Lithology	Texture	Main pore-type occurrence	Porosity (%)	Permeability (mD)	Resolution	Pixels
[A]	X560	Spherulite	Wackestone	Vug and moldic	18.1	13.5	2.5X	300×225
[B]	X570	Spherulite	Wackestone	Vug	13.1	2.88	2.5X	300×225
[C]	X575	Arborescent STR	Packstone	Interelement and vug	19.2	135	10X	300×225
[D]	X580	Stromatolite	Packstone	Intercrystalline, interelement, intraelement, and intracrystalline	16.8	354	5X	300×225
[E]	X585	Arborescent STR	Grainstone	Interelement, intraelement, and fracture	17.8	376	5X	300×225
[F]	X590	Spherulithite	Crystalline	Intercrystalline	11.2	2.04	5X	300×225
[G]	X595	Laminite	Crystalline	Intercrystalline, interparticle, and intraparticle	8.6	0.92	5X	300×225
[H]	X600	Laminite	Crystalline	Moldic	6.6	0.21	5X	300×225
[I]	X610	Spherulithite	Crystalline	Moldic	10.3	0.17	5X	300×225
[J]	X615	Spherulithite	Crystalline	Intercrystalline, interelement, and intraelement	5.8	0.02	5X	300×225

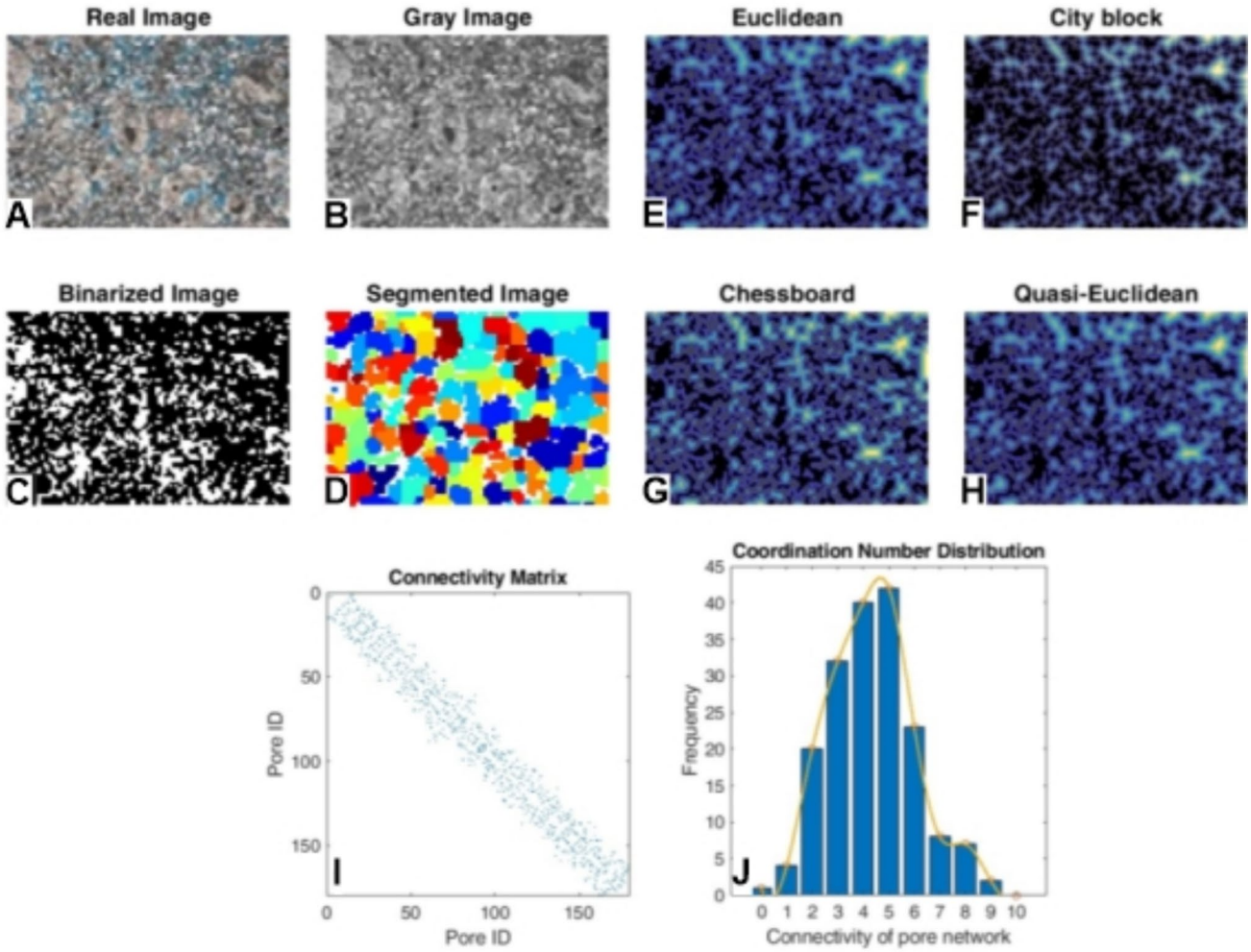

Fig. 7 Digital characterization of carbonate pore systems for the sample's two-dimensional pore structures [A]. **a** Real image, **b** Grayscale image conversion, **c** Binarized image, **d** Segmented image. Four different forms of distance functions from **e** to **h**, **i** Graph of the sparse adjacency matrix's connectivity network, **j** Histogram of coordination number distribution

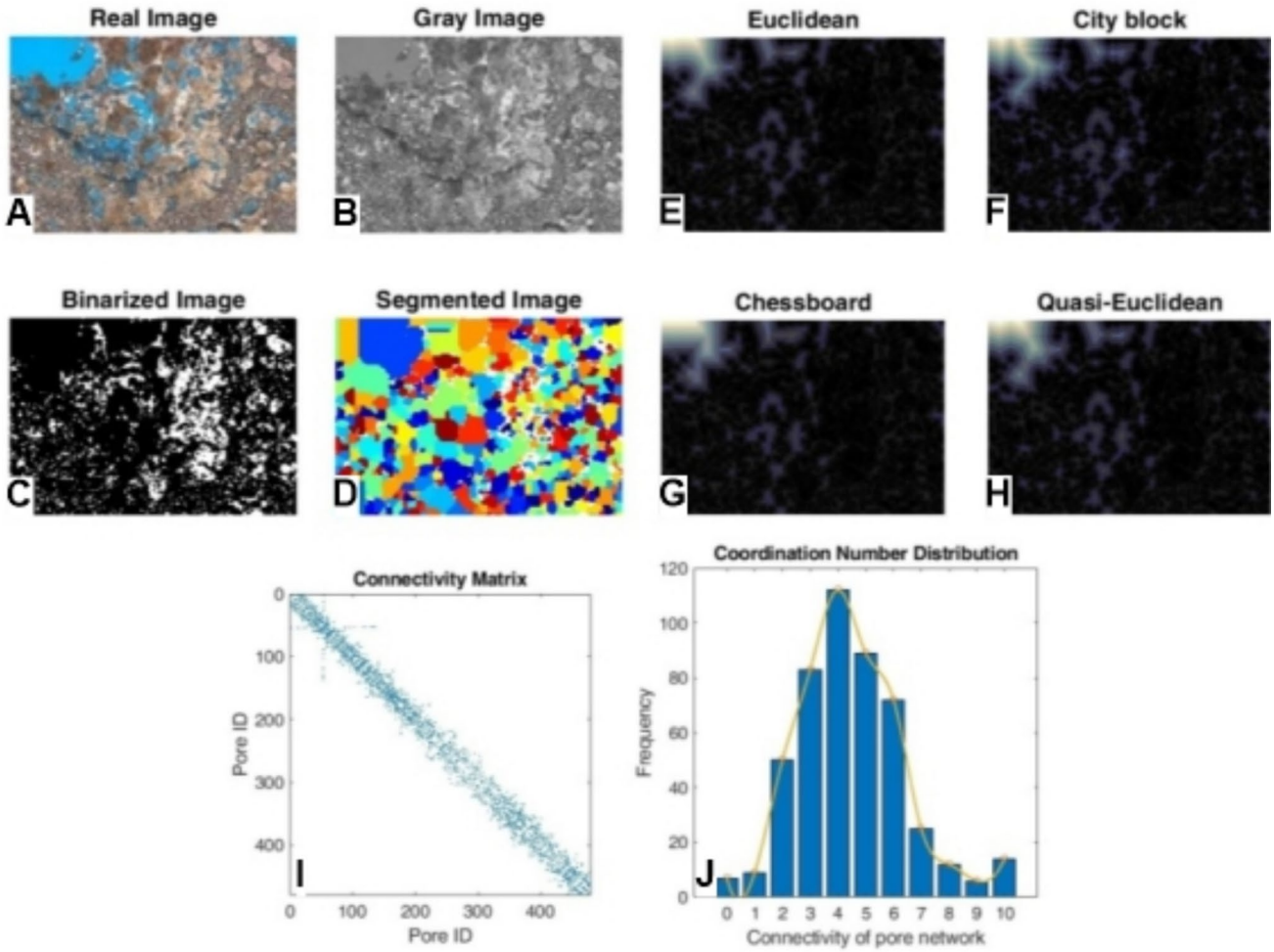

Fig. 8 Digital characterization of carbonate pore systems for the sample's two-dimensional pore structures [B]

The histogram shows a right-skewed unimodal distribution with a peak abundance frequency of 2 connections between the pores. This level is the lowest of connectivity observed among the other samples. Figure 11J illustrates the high frequency of pores that have no connectivity.

Figure 12 displays the results of sample [F] and sample [A], which have distinct textures but belong to the same lithology. These results, as shown in Table 3, are highly comparable. Figure 13 displays the results of analyzing the digital photographs of the sample's pore architectures [G]. This highly heterogeneous sample exhibits an scattering of points in the connection graph representing the sparse adjacency matrix (Fig. 13I).

The existence of round-to-round oval particles, composed of concentric layers (cortex) consisting primarily of calcite around a central core (sand grains or bioclasts) accounts for this variation. Figure 13I shows that the connected pore network's histogram had a bimodal distribution, with two clear peaks showing connections between pores 3 and 6. An incipient lamination may also influence these linkages, indicating the existence of underdeveloped strata where the original micritic matrix has partially disintegrated and quartz has replaced it.

Figure 14 displays the obtained [H] measurements. Following the segmentation stage, there is a noticeable clustering of the pore network at the lower part of the image, as observed through several distance metrics (Fig. 14E–H). When comparing samples [H] and [I], it is evident that they possess distinct lithologies due to a transition zone characterized by spherulite-laminite. However, they share the same crystalline texture and moldic pore type. There were no notable variations in the arrangement of dots in the pore connectivity matrix (Fig. 14I). It is essential to highlight that the connectivity network histogram for sample [H] is similar to sample [A]. Both samples show moldic porosity, no pores with zero connections, and a unimodal distribution with a peak at three connections and symmetry.

Figures 15 and 16 display the outcomes of samples [I] and [J], respectively. After segmentation (see Fig. 15A–D), the results show that the distance metrics correctly show

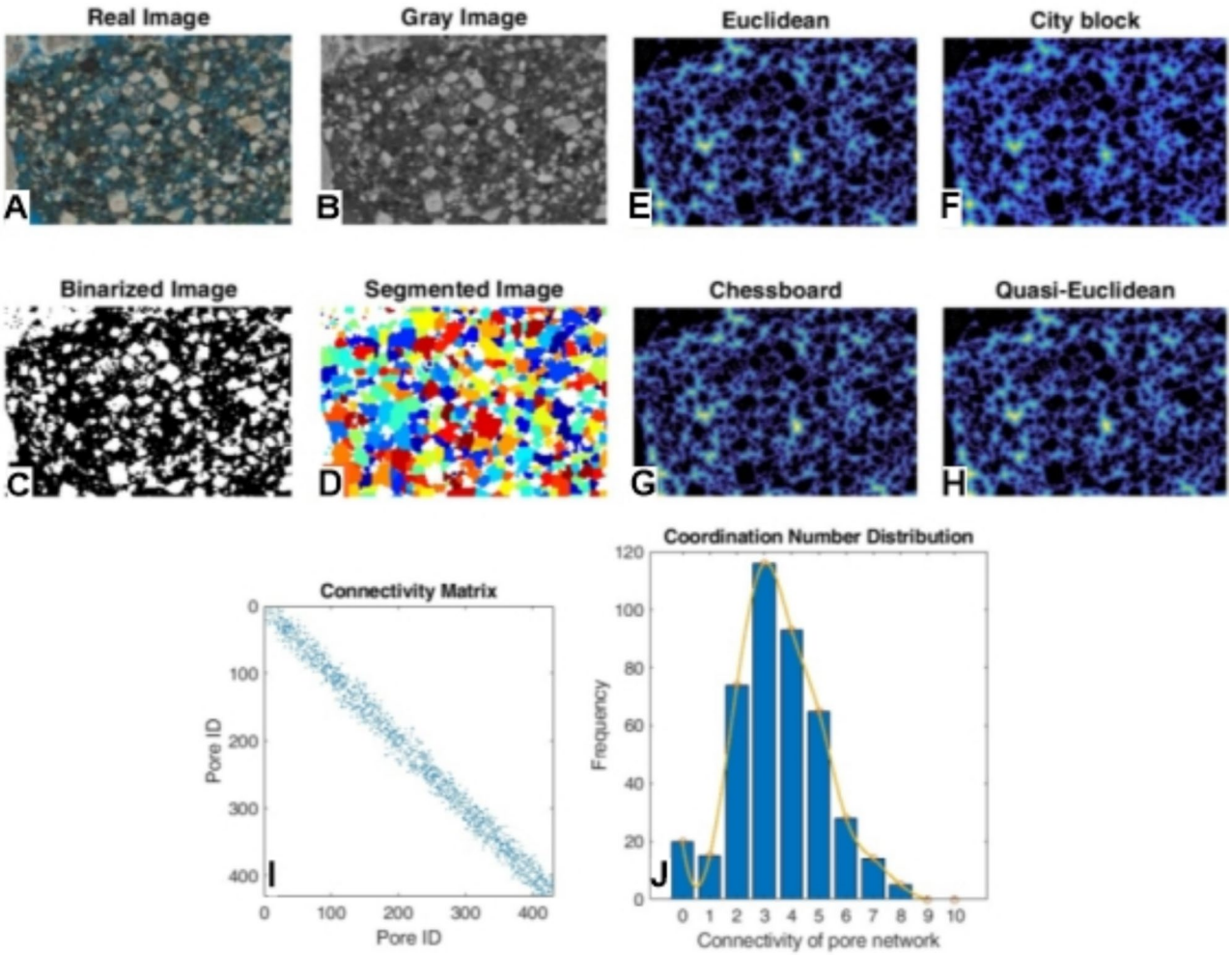

Fig. 9 Digital characterization of carbonate pore systems for the sample's two-dimensional pore structures [C]

the pore network, especially near the stromatolites. To show how well the chessboard measure works, consider how the stromatolites connect the pore network to different parts of the sample (see Fig. 15E–H).

Figure 15I illustrates the sparsely connected matrix representing the pores in the sample [I]. The figure displays a dispersed arrangement of dots. The sparse matrix indicates that most pores exhibit robust connectivity, whereas the presence of zeros signifies limited or absent connections between numerous pairs of pores. The distribution of dots is not uniform but rather concentrated in specific areas, suggesting the presence of clusters of interconnected pores.

The existence of specific individual dots with a higher quantity of connections signifies diversity in connectivity and mirrors diversity in the porous composition of the stromatolites. Figure 15J shows the skewed, one-modal distribution of the data about the number of connections between pores in the sample [I]. This distribution is not symmetrical.

Additionally, the tail exhibits a rightward skewed distribution. Lower values to the left of the central peak (representing four connections) predominantly display pores with fewer connections. Furthermore, the tail exhibits a rightward skewed distribution. The majority of pores have multiple connections. Nevertheless, there is a slight dispersion of data towards the right, indicating a few pores exhibiting a significantly higher connection. The asymmetry in the pores' connectivity indicates heterogeneity in their interconnections. Specifically, a small number of pores with a high level of connectivity (eight to ten connections) significantly impact the distribution's tail.

Because Fig. 16 lacks the pores typically found in connections, it resembles Fig. 14. The histogram in Fig. 16J, which also features a prominent peak representing three connections, clearly demonstrates this. Nevertheless, [J] exhibits very minimal values for porosity and permeability.

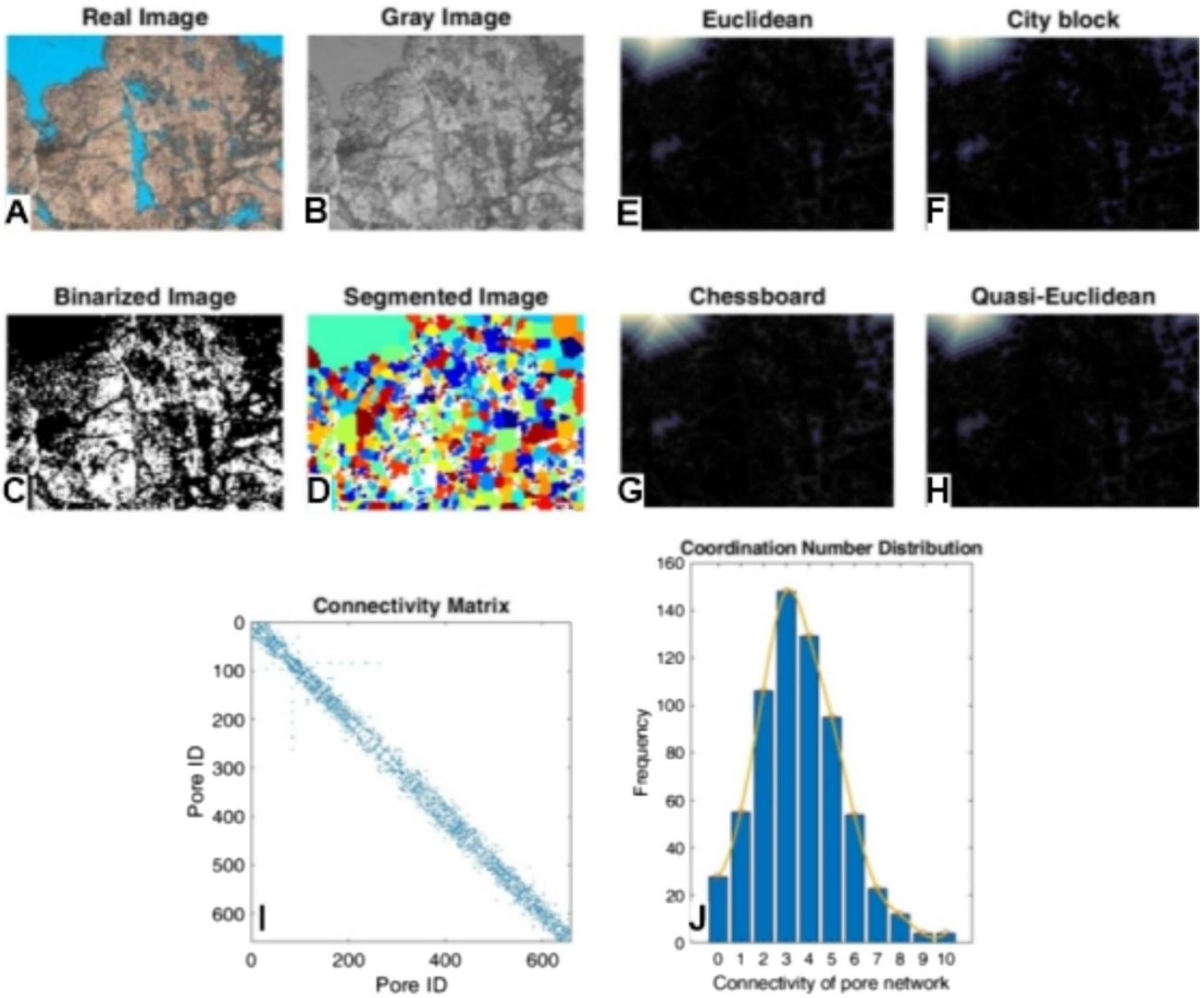

Fig. 10 Digital characterization of carbonate pore systems for the sample's two-dimensional pore structures [D]

Conclusions

This study highlights the critical role of distance metrics in evaluating pore network interconnectivity within pre-salt carbonate rocks, particularly in the context of reservoir characterization. By employing Euclidean, quasi-Euclidean, city-block, and chessboard distance metrics, we were able to differentiate between pores and throats, thereby offering a more precise and comprehensive examination of the microstructure in the samples analyzed. The city-block metric, in particular, proved effective in distinguishing these structures, accurately representing the interconnectedness of the pore network.

The Euclidean distance emerged as the most suitable method for assessing pore connectivity and infiltration characteristics. Its ability to measure the shortest, straight-line distance between two points provides a realistic representation of fluid movement through the pore network, making it ideal for evaluating reservoirs with high connectivity and potential for good infiltration characteristics. The quasi-Euclidean distance, while an approximation, strikes a balance between accuracy and computational efficiency, making it appropriate for moderate connectivity reservoirs, especially in large or complex systems where exact Euclidean calculations may be computationally intensive.

Conversely, the city-block distance, which restricts movement to orthogonal directions, is less accurate for natural porous media, as it does not account for diagonal pathways. This limitation may lead to an underestimation of pore connectivity and, consequently, an inaccurate assessment of infiltration characteristics. The chessboard distance, which treats diagonal and orthogonal movements equally, can be useful in highly interconnected networks. However, it risks oversimplifying fluid movement in less uniform

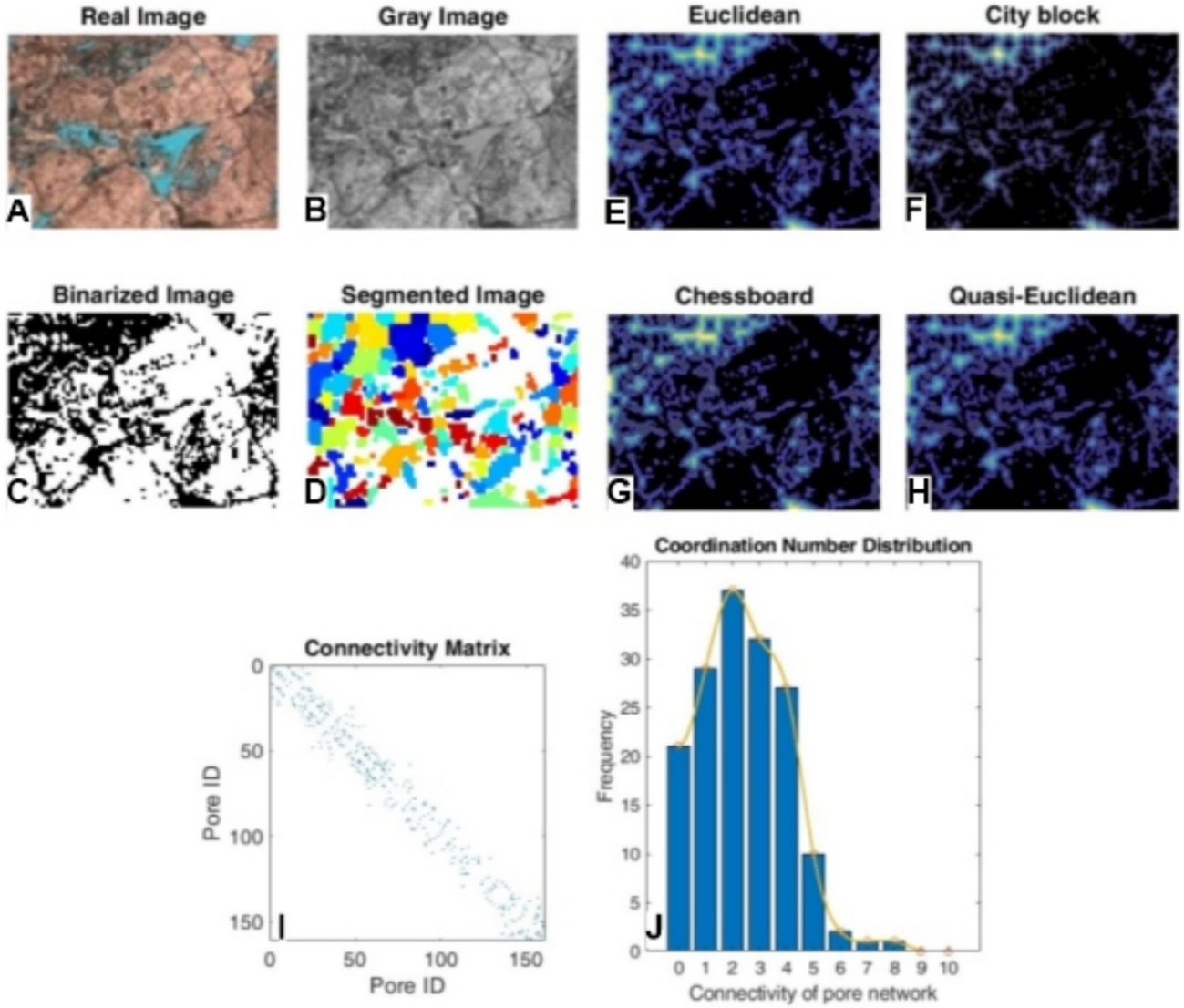

Fig. 11 Digital characterization of carbonate pore systems for the sample's two-dimensional pore structures [E]

pore networks, potentially leading to an overestimation of connectivity.

These findings are crucial for several applications, including reservoir characterization, enhanced oil recovery (EOR), carbon capture and storage (CCS), groundwater flow analysis, and materials research. The detailed understanding of pore structure and connectivity gained through this study is instrumental in optimizing these applications by informing decisions related to porosity, permeability, fluid flow, and overall reservoir performance.

Furthermore, the results underscore the importance of carefully selecting and integrating appropriate distance metrics to accurately characterize the microscopic structures of carbonate rocks. The combination of metrics used in this study allowed for a thorough evaluation of pore network connectedness, revealing patterns and distributions that are key to understanding the petrophysical properties of the rocks.

It is recommended that future studies consider the number of interconnections between pores in carbonate reservoir samples when using models such as the Kozeny equation to predict petrophysical parameters like permeability. Additionally, exploring the relationship between pore connectivity and tortuosity in these reservoirs could lead to a deeper understanding of fluid dynamics, thereby aiding in the optimization of carbonate reservoir exploration and production.

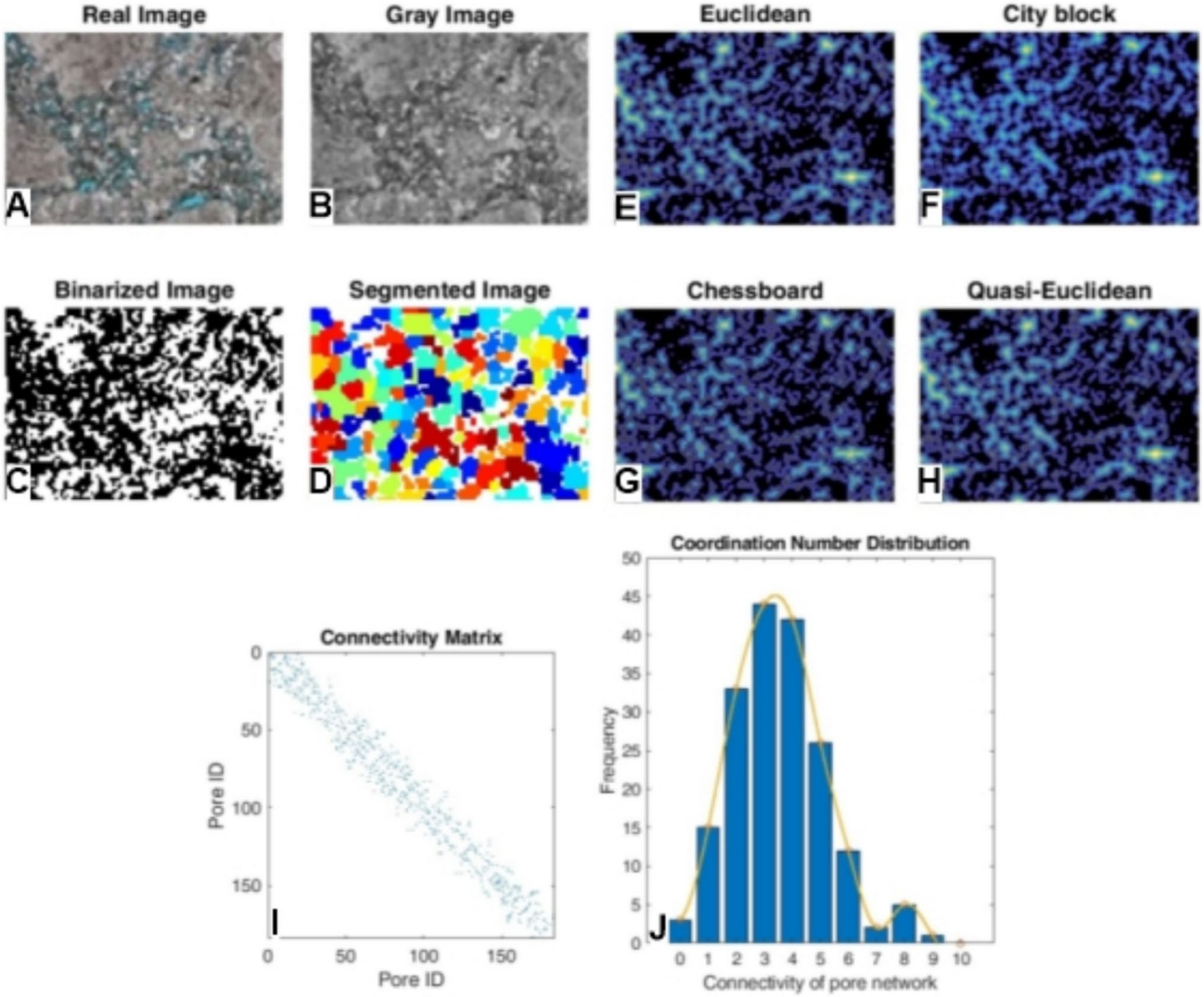

Fig. 12 Digital characterization of carbonate pore systems for the sample's two-dimensional pore structures [F]

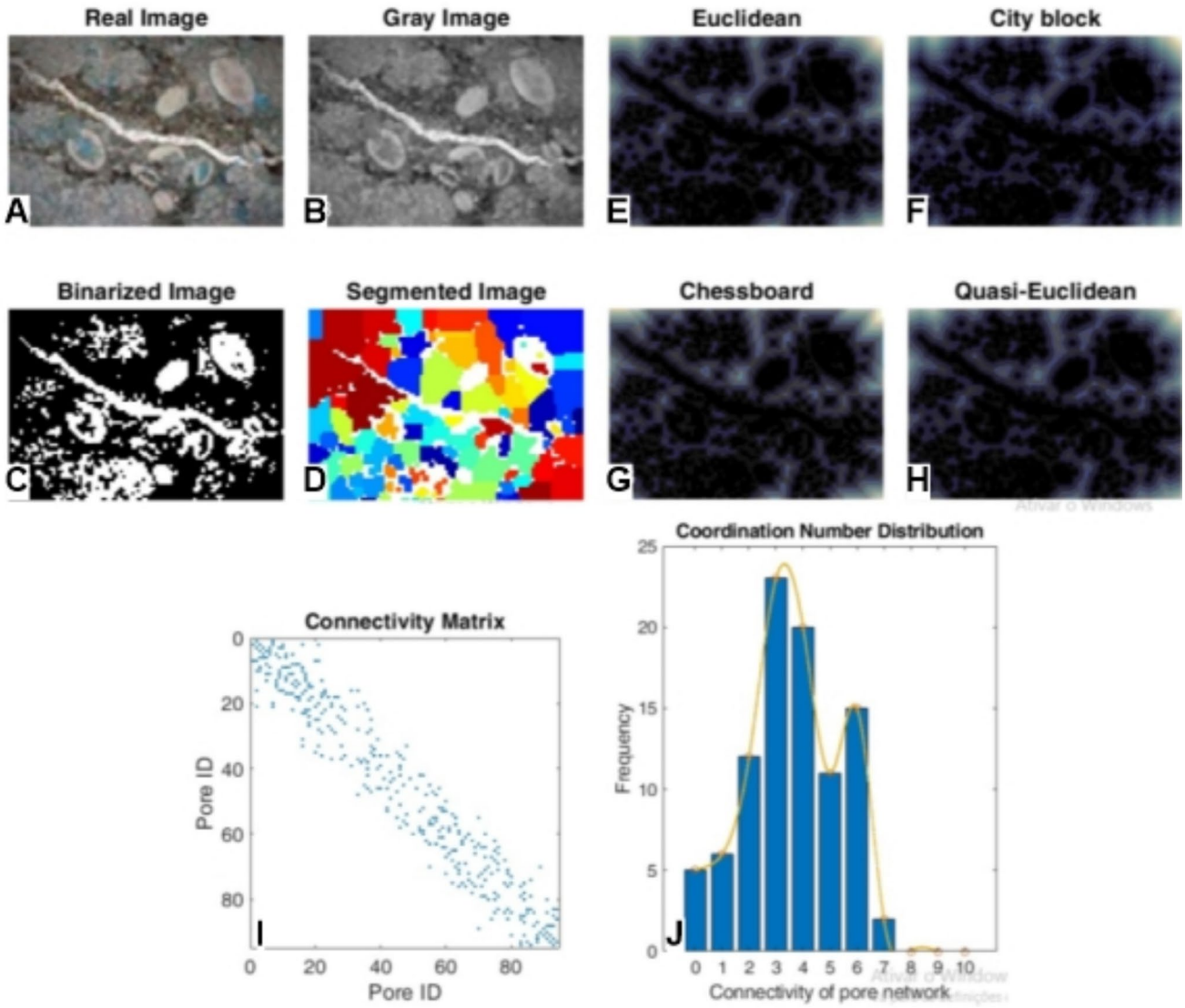

Fig. 13 Digital characterization of carbonate pore systems for the sample's two-dimensional pore structures [G]

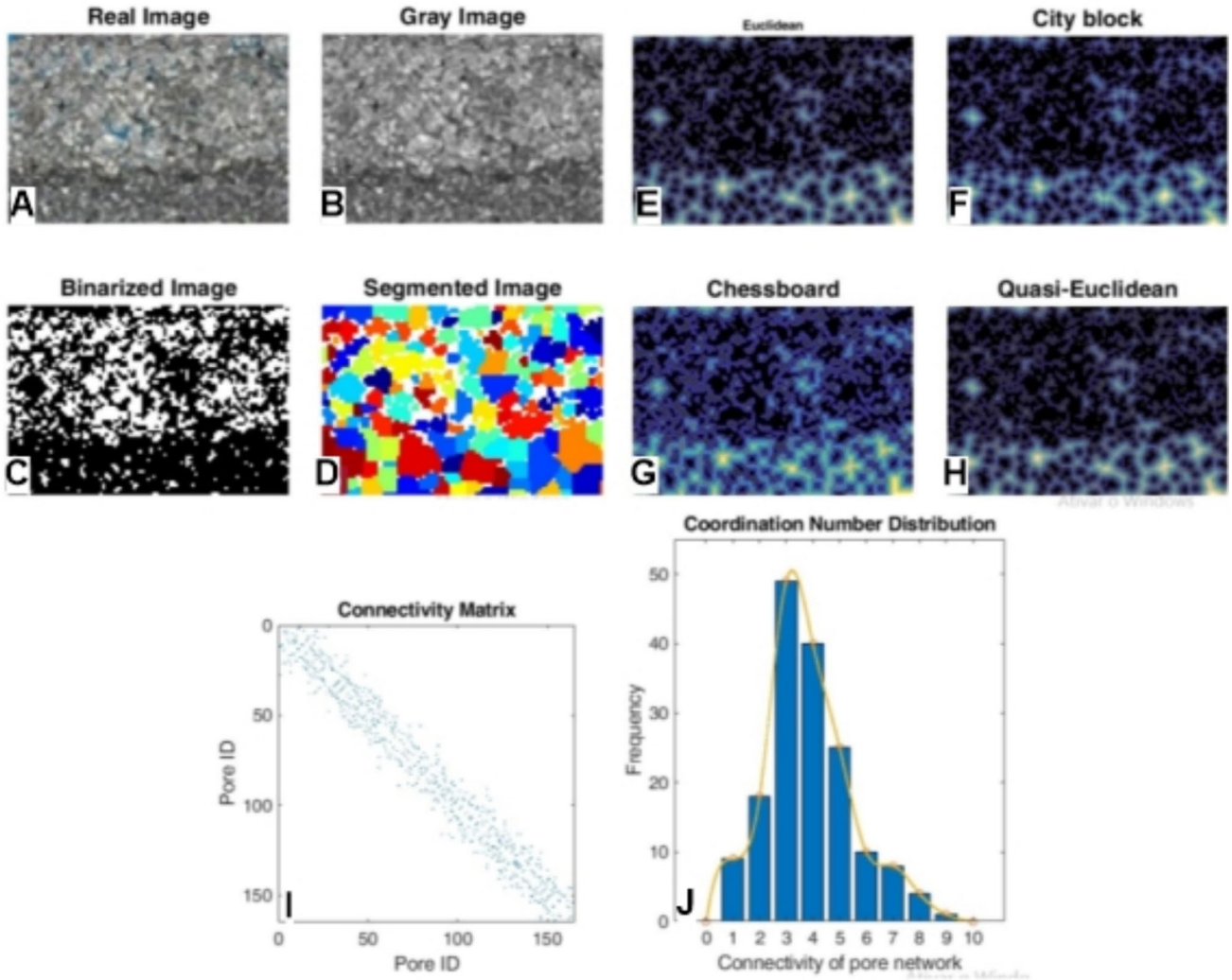

Fig. 14 Digital characterization of carbonate pore systems for the sample's two-dimensional pore structures [H]

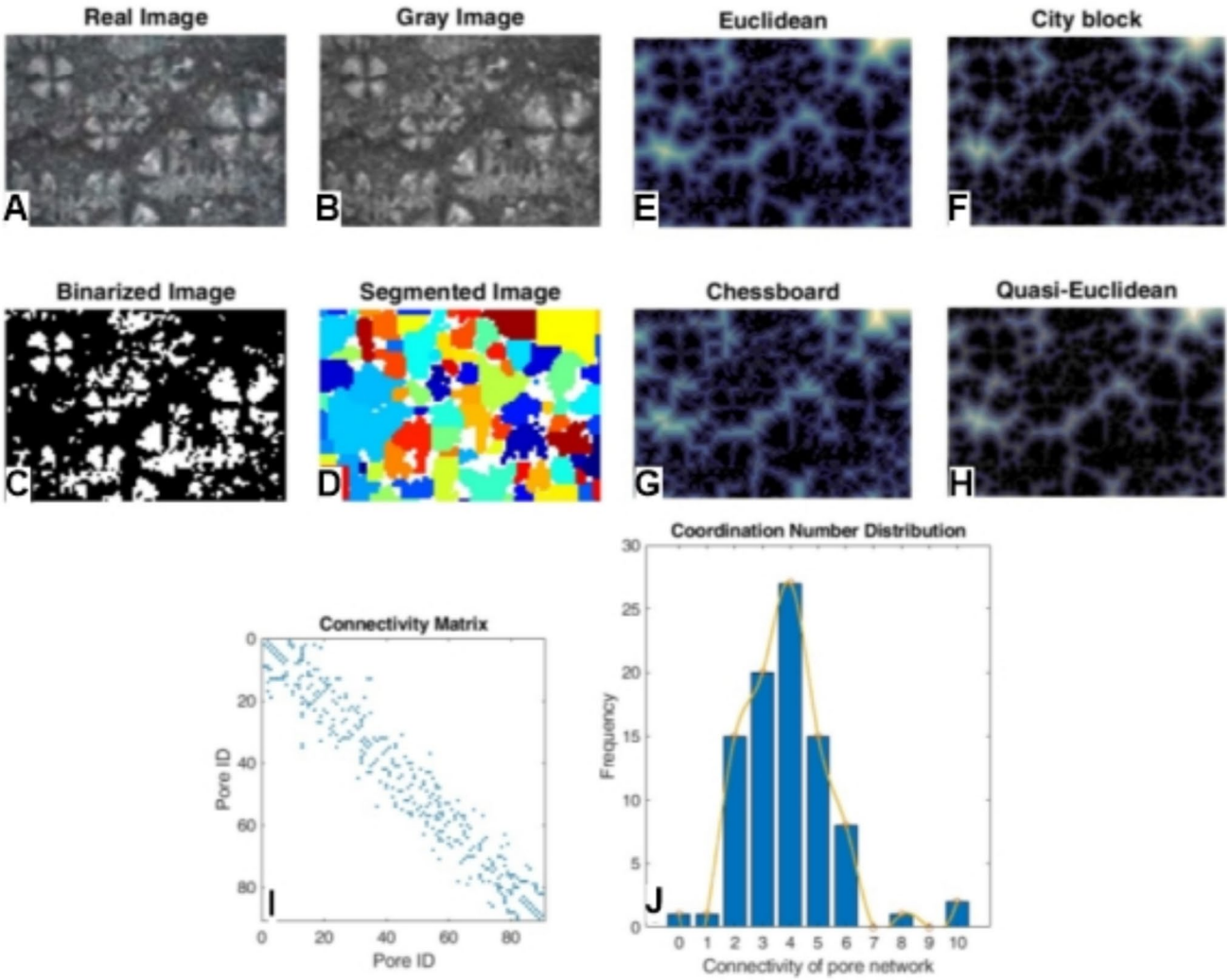

Fig. 15 Digital characterization of carbonate pore systems for the sample's two-dimensional pore structures [I]

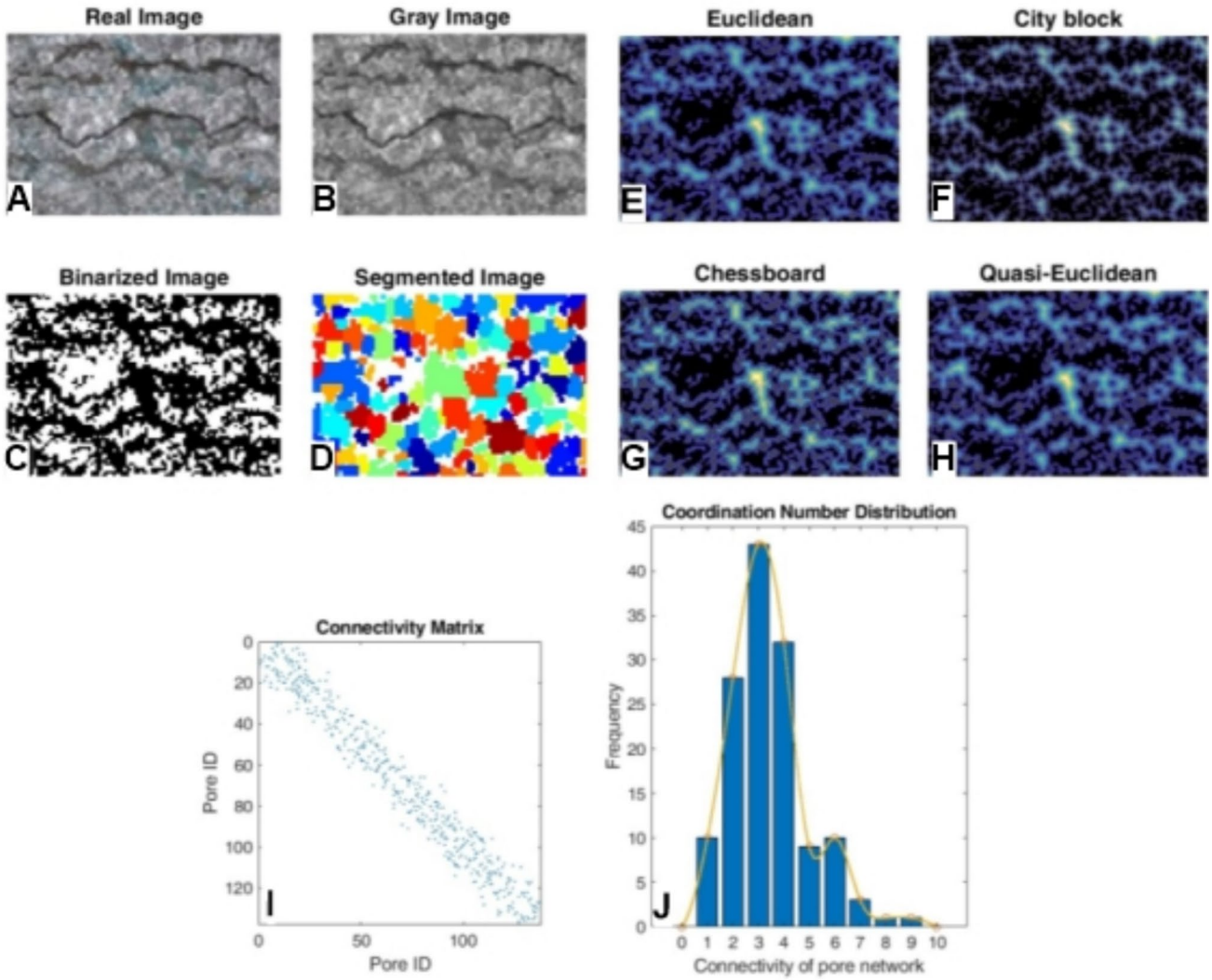

Fig. 16 Digital characterization of carbonate pore systems for the sample's two-dimensional pore structures [J]

Acknowledgements The authors would like to thank the universities (UFRJ, UFPA, and UENF) that provided computational support. Their special thanks go to the Brazilian Ministry of Education (CAPES) for supporting the work of the first author, the National Council for Scientific and Technological Development (CNPq) for funding the work of the third author, and Petrobras for financing the work of the fourth author through its Human Resources Program (PRH-226). We also sincerely thank the Brazilian National Petroleum Agency (ANP) for providing the dataset.

Author contributions All authors reviewed the manuscript.

Data availability No datasets were generated or analysed during the current study.

Declarations

Conflict of interest The authors declare no competing interests.

References

Alatrash H, Velledits F (2024) Comparing petrophysical properties and pore network characteristics of carbonate reservoir rocks using micro X-ray tomography imaging and microfacies analyses. GEM Int J Geomath 15(1):1. https://doi.org/10.1007/s13137-023-00243-8

Azerêdo AC, Duarte LV, Silva AP (2021) The challenging carbonates from the pre-salt reservoirs offshore Brazil: facies, palaeoenvironment, and diagenesis. J S Am Earth Sci 108:103202. https://doi.org/10.1016/j.jsames.2021.103202

Bernabe Y, Li M, Maineult A (2010) Permeability and pore connectivity: a new model based on network simulations. J Geophys Res Solid Earth. https://doi.org/10.1029/2010JB007444

Borghi L, Corbett PWM (2013) Lacustrine carbonates—for the purpose of reservoir characterization, are they different? In: Annual Offshore Technology Conference, Rio de Janeiro, Paper Number: OTC-24482-MS. https://doi.org/10.4043/24482-MS

Bultreys T, Van Hoorebeke L, Cnudde V (2015) Multi-scale, micro-computed tomography-based pore network models to simulate

drainage in heterogeneous rocks. Adv Water Resour 78:36–49. https://doi.org/10.1016/j.advwatres.2015.02.003
Bultreys T, De Boever W, Cnudde V (2016) Imaging and image-based fluid transport modeling at the pore scale in geological materials: a practical introduction to the current state of the art. Earth Sci Rev 155:93–128. https://doi.org/10.1016/j.earscirev.2016.02.001
Da Rocha HO, Da Costa JLS, Carrasquilla AAG, Carrasco AMV (2019) Petrophysical characterization using well log resistivity and rock grain specific surface area in a fractured carbonate pre-salt reservoir in the Santos Basin, Brazil. J Petrol Sci Eng 183(24):106372. https://doi.org/10.1016/j.petrol.2019.106372
Dong H, Blunt MJ (2009) Pore-network extraction from micro-computerized-tomography images. Phys Rev E 80(3):036307
Dunham RJ (1962) Classification of carbonate rocks according to depositional texture. In: Ham WE (ed) Classification of carbonate rocks. Tulsa, vol. 1. American Association of Petroleum Geologists, Memoir, pp. 108–122
Faria DLP, Dos Reis AT, Souza OG Jr (2017) Three-dimensional stratigraphic-sedimentological forward modeling of an Aptian carbonate reservoir deposited during the SAG stage in the Santos basin Brazil. Mar Pet Geol 88:676–695. https://doi.org/10.1016/j.marpetgeo.2017.09.013
Ghanbarnejad Moghanloo H, Riahi MA (2023) Integrating watershed segmentation algorithm and supervised Bayesian classification for the assessment of petrophysical parameters, pore properties, and lithofacies: a case study from Abadan Plain. SW Iran Earth Sci Inform 16(4):3913–3930. https://doi.org/10.1007/s12145-023-01129-x
Gharbi O, Blunt MJ (2012) The impact of wettability and connectivity on relative permeability in carbonates: a pore network modeling analysis. Water Resour Res 48:W12513. https://doi.org/10.1029/2012WR011877
Gonzales RC, Woods RE, Eddins SL (2004) Digital image processing using MATLAB. Pearson Prentice Hall, pp. 609
Gostick JT (2017) Versatile and efficient pore network extraction method using marker-based watershed segmentation. Phys Rev E 96(2):023307. https://doi.org/10.1103/PhysRevE.96.023307
Huang W, Cui Y, Xu F, Meng Z, Guo S, Zhang C (2021) An innovative approach to permeability estimation of the fractured-vuggy carbonate reservoirs based on 2D images. J Petrol Sci Eng 199:108293. https://doi.org/10.1016/j.petrol.2020.108293
Ioannidis MA, Chatzis I (2000) A dual-network model of pore structure for vuggy carbonates. In: International Symposium of the Society of Core Analysts. Abu Dhabi, Paper SCA 2000-09-(1)
Jahari AF, Shafian SRM, Husin H, Razali N, Irawan S (2021) Quantification method of suspended solids in micromodel using image analysis. J Pet Explor Prod Technol 11(5):2271–2286. https://doi.org/10.1007/s13202-021-01153-x
Jivkov AP, Hollis C, Etiese F, McDonald SA, Withers PJ (2013) A novel architecture for pore network modeling with applications to the permeability of porous media. J Hydrol 486:246–258. https://doi.org/10.1016/j.jhydrol.2013.01.045
Khan NM, Ma L, Cao K, Hussain S, Ali A, Liu W, Xu Y (2022) Evaluating the thermal-cooling-induced effects on the Ambela granite properties (from Pakistan) using experimental and image processing techniques. Bull Eng Geol Environ 81(12):506. https://doi.org/10.1007/s10064-022-03019-w
Kumar PA, Anuradha B (2017) Estimating reflectivity of DWR images by analyzing different color spaces through distance measures. Adv Comput Sci Technol 10(8):2191–2200
Land LS (1985) The origin of massive dolomite. J Geol Educ 33(2):112–125
Liu H, Rodrigues S, Shi F, Esterle J, Manlapig E (2017) Coal washability analysis using X-ray tomographic images for different lithotypes. Fuel 209:162–171. https://doi.org/10.1016/j.fuel.2017.07.104
Lucia FJ (1995) Rock-fabric petrophysical classification of carbonate pore space for reservoir characterization. AAPG (Am Assoc Pet Geol) Bull 79(9):1275–1300
Macedo JM (1989) Tectonic evolution of the Santos Basin and adjacent continental areas. Petrobras Geosci Bull Rio De Janeiro 3(3):159–173 (**in Portuguese**)
Mandzhieva R, Subhankulova R (2021) Practical aspects of absolute permeability finding for the lattice Boltzmann method and pore network modeling. Physica A 582:126249. https://doi.org/10.1016/j.physa.2021.126249
Maurer CR Jr, Qi R, Raghavan V (2003) A linear time algorithm for computing exact euclidean distance transforms of binary images in arbitrary dimensions. IEEE Trans Pattern Anal Mach Intell 25(2):265–270. https://doi.org/10.1109/TPAMI.2003.1177156
Meyer F (1994) Topographic distance and watershed lines. Signal Process 38(1):113–125
Mio E, Chang H, Corrêa F (2005) Integração de métodos geofísicos na modelagem crustal da Bacia de Santos. Revista Brasileira de Geofisica 23(3):275–284. https://doi.org/10.1590/S0102-261X2005000300006. (**in Portuguese**)
Modica CJ, Brush ER (2004) Postrift sequence stratigraphy, paleogeography, and fill history of the deepwater Santos Basin, offshore Southeast Brazil. AAPG Bull 88(7):923–945. https://doi.org/10.1306/01220403043
Moreira JLP, Madeira CV, Gil JA, Machado MAP (2007) Bacia de Santos. Boletim De Geociências Da Petrobras 15(2):531–549 (**in Portuguese**)
Neto IAL, Ceia MA, Missagia RM, Oliveira GL, Santos VH, Paranhos RP, Archilha NL (2018) Testing and evaluation of 2D/3D digital image analysis methods and inclusion theory for microporosity and S-wave prediction in carbonates. Mar Pet Geol 97:592–611. https://doi.org/10.1016/j.marpetgeo.2018.08.004
Otsu N (1979) A threshold selection method from gray-level histograms. IEEE Trans Syst Man Cybern 9(1):62–66
Rabbani A, Ayatollahi S (2015) Comparing three image processing algorithms to estimate the grain-size distribution of porous rocks from binary 2D images and sensitivity analysis of the grain overlapping degree. Spec Top Rev Porous Media Int J 6(1):71–89. https://doi.org/10.1615/SpecialTopicsRevPorousMedia.v6.i1.60
Rabbani A, Jamshidi S, Salehi S (2014) An automated simple algorithm for realistic pore network extraction from micro-tomography images. J Petrol Sci Eng 123:164–171. https://doi.org/10.1016/j.petrol.2014.08.020
Rabbani A, Ayatollahi S, Kharrat R, Dashti N (2016) Estimation of 3-D pore network coordination number of rocks from watershed segmentation of a single 2-D image. Adv Water Resour 94:264–277. https://doi.org/10.1016/j.advwatres.2016.05.020
Raoof A, Hassanizadeh SM (2010) A new method for generating pore-network models of porous media. Transp Porous Media 81(3):391–407. https://doi.org/10.1007/s11242009-9412-3
Riding R, Liang L (2005) Geobiology of microbial carbonates: metazoan and seawater saturation state influences on secular trends during the Phanerozoic. Paleogeogr Paleoclimatol Paleoecol 219:101–115. https://doi.org/10.1016/j.palaeo.2004.11.018
Rocha H, Carrasquila A (2021) 2D digital image segmentation techniques to characterize the porosity of carbonate rocks in Brazilian pre-salt. In: 82nd EAGE Annual Conference and Exhibition (Vol. 2021, No. 1, pp. 1–5). European Association of Geoscientists and Engineers. https://doi.org/10.3997/2214-4609.202112684
Rosenfeld A, Pfaltz JL (1966) Sequential operations in digital picture processing. J ACM (JACM) 13(4):471–494
Sheppard AP, Sok RM, Averdunk H (2004) Techniques for image enhancement and segmentation of tomographic images of porous

materials. Physica A 339(1):145–151. https://doi.org/10.1016/j.physa.2004.03.057

Singh A, Rabbani A, Regenauer-Lieb K, Armstrong RT, Mostaghimi P (2021) Computer vision and unsupervised machine learning for pore-scale structural analysis of fractured porous media. Adv Water Resour 147:103801. https://doi.org/10.1016/j.advwatres.2020.103801

Sok RM, Knackstedt MA, Sheppard AP, Pinczewski WV, Lindquist WB, Venkatarangan A, Paterson L (2002) Direct and stochastic generation of network models from tomographic images; effect of topology on residual saturations. Transp Porous Media 46(2–3):345–371

Sok R, Varslot T, Ghous A, Latham S, Sheppard A, Knackstedt M (2010) Pore scale characterization of carbonates at multiple scales: integration of micro-CT BSEM and FIBSEM. Petrophysics 51(6):379–387

Sonka M, Hlavac V, Boyle R (2014) Image processing, analysis, and machine vision. Cengage Learning, Australia, p 930

Strugale M, Lima BEM, Day C, Omma J, Rushton J, Olivito JPR, Cartwright J (2025) Diagenetic products, settings and evolution of the pre-salt succession in the Northern Campos Basin, Brazil. Geol Soc Lond Spec Publ 548(1):2021. https://doi.org/10.1144/SP548-2023-9

Tawfeeq YJ, Al-Sudani JA (2020) Digital rock analysis: an alternative method to predict petrophysical properties case study from Mishrif Formation. Iraqi Geol J 53:34–55. https://doi.org/10.46717/igj.53.2c.4Rs-2020-09-04

Valentin M, Bom C, Compan A, Correia M, de Jesus C, Souza A, de Albuquerque A, de Albuquerque M, Faria E (2018) Estimation of permeability and effective porosity logs using deep autoencoders in borehole image logs from the Brazilian pre-salt carbonate. J Petrol Sci Eng 170(2018):315–330. https://doi.org/10.1016/j.petrol.2018.06.038

Van der Land C, Wood R, Wu K, Van Dijke MI, Jiang Z, Corbett PW, Couples G (2013) Modeling the permeability evolution of carbonate rocks. Mar Pet Geol 48:1–7. https://doi.org/10.1016/j.marpetgeo.2013.07.006

Wang H, Ge S, Lipton Z, Xing EP (2019) Learning robust global representations by penalizing local predictive power. Adv Neural Inform Process Syst 32

Wennberg OP, Ramalho FDO, Mafia MV, Lapponi F, Chandler AS, Cartesio LG, Hunt DW (2023) The characteristics of natural open fractures in acoustic borehole image logs from the pre-salt Barra Velha formation, Santos Basin, Brazil. J Struct Geol 167:104794. https://doi.org/10.1016/j.jsg.2023.104794

Wright DT (1999) The role of sulphate-reducing bacteria and cyanobacteria in dolomite formation in distal ephemeral lakes of the Coorong region, South Australia. Sediment Geol 126(1–4):147–157